

# A comparison of simulation tools for Muon-Induced X-ray Emission (MIXE) in thin films: a study case with lithium batteries

Maxime Lamotte<sup>a</sup>, Michael W. Heiss<sup>a</sup>, Thomas Prokscha<sup>a</sup>, Alex Amato<sup>a</sup>

<sup>a</sup>*PSI Center for Neutron and Muon Sciences (CNM), Paul Scherrer Institute, 5232 Villigen PSI, Switzerland*

---

## Abstract

We present a comparative study of three Monte Carlo simulation frameworks—SRIM, GEANT4, and PHITS—for modeling the transport, stopping, and atomic cascade of negative muons in micrometer-scale, multilayer systems relevant to Muon-Induced X-ray Emission (MIXE) experiments at the Paul Scherrer Institute (PSI). Using a lithium-ion battery as a benchmark target, simulated implantation profiles are compared with experimental data from the GIANT spectrometer. All three codes reproduce the overall muon depth distributions with good consistency, even across sharp density contrasts. SRIM provides reliable implantation estimates for compact geometries, whereas PHITS reproduces GEANT4 results with comparable accuracy and additionally generates muonic X-ray spectra. These spectra, however, exhibit a systematic energy offset in the K-line transitions of medium- and high-Z elements relative to theoretical and experimental values. Despite this bias, PHITS accurately captures relative intensities and spectral shapes, enabling element-specific line identification. The results demonstrate that SRIM and PHITS constitute practical tools for rapid estimation of muon implantation and stopping profiles, and that PHITS holds strong potential for predictive MIXE spectroscopy once its transition-energy bias is corrected.

**Keywords:** Muon-Induced X-ray Emission, MIXE, PHITS, GEANT4, SRIM, muonic atoms, lithium batteries, Monte Carlo simulation, muon capture, X-ray spectroscopy

---

## 1. Introduction, MIXE at Paul Scherrer Institute

Muon-Induced X-ray Emission (MIXE) has long been employed to probe atomic-scale properties such as nuclear size, shape and charge distribution [1, 2]. The field originated in the 1960s–1970s through precision muonic-atom spectroscopy, where measurements of transition energies revealed fine nuclear-structure effects beyond the reach of conventional X-ray methods. In the 1980s, pioneering work at the Swiss Institute for Nuclear Research (SIN)—now the Paul Scherrer Institute (PSI)—extended MIXE to non-destructive elemental analysis of cultural and geological samples

[3, 4]. With PSI’s high-intensity continuous muon beams, generated at the High-Intensity-Proton-Accelerator-Facility HIPA [5], the Swiss Muon Source (S $\mu$ S) now enables routine MIXE studies of bulk specimens using the GIANT HPGe array [6] (Fig. 1). Recent efforts within the Swiss National Science Foundation (SNSF) interdisciplinary research program DEEP $\mu$  (SNSF Sinergia grant 193691) have demonstrated depth-resolved, isotope-specific analysis of materials ranging from archaeological artifacts to energy-storage devices, motivating the development of reliable simulation tools for experiment design and data interpretation.

In the MIXE technique at PSI, negative muons from the  $\pi$ E1 beamline are implanted in a sample with tuneable momenta —from 15 to 60 MeV/c—corresponding to a penetration range up to 3 g/cm<sup>2</sup>. Momenta of up to 125 MeV/c (58 MeV kinetic energy), and therefore a deeper penetration of the sample, can be achieved in the future by modifying the  $\mu$ E1 beamline. This specific beamline delivers muons originating from in-flight pion decay extracted from the thick (E) graphite target [5], in a long superconducting magnet. Momenta between 60 to 125 MeV/c can be selected, allowing to probe from millimeters to about 10 centimeters in aluminium.

By varying the  $\pi$ E1 beam momentum, a depth scan analysis can be performed in the surface vicinity of the sample to millimeters deep within the bulk of the sample. The depth resolution ranges between a few microns and 1 mm, depending on the momentum spread ( $\Delta p/p$ ) of the beam, the density of the material, and the implantation depth. The beam has a typical waist diameter of about 2 cm which is also momentum dependent, as lower energy muons are more likely to experience Molière scattering in entrance detector, insulation windows and air. Passive collimation can be set up to reduce the beam size, at the expense of decreased implantation rates and longer acquisition times.

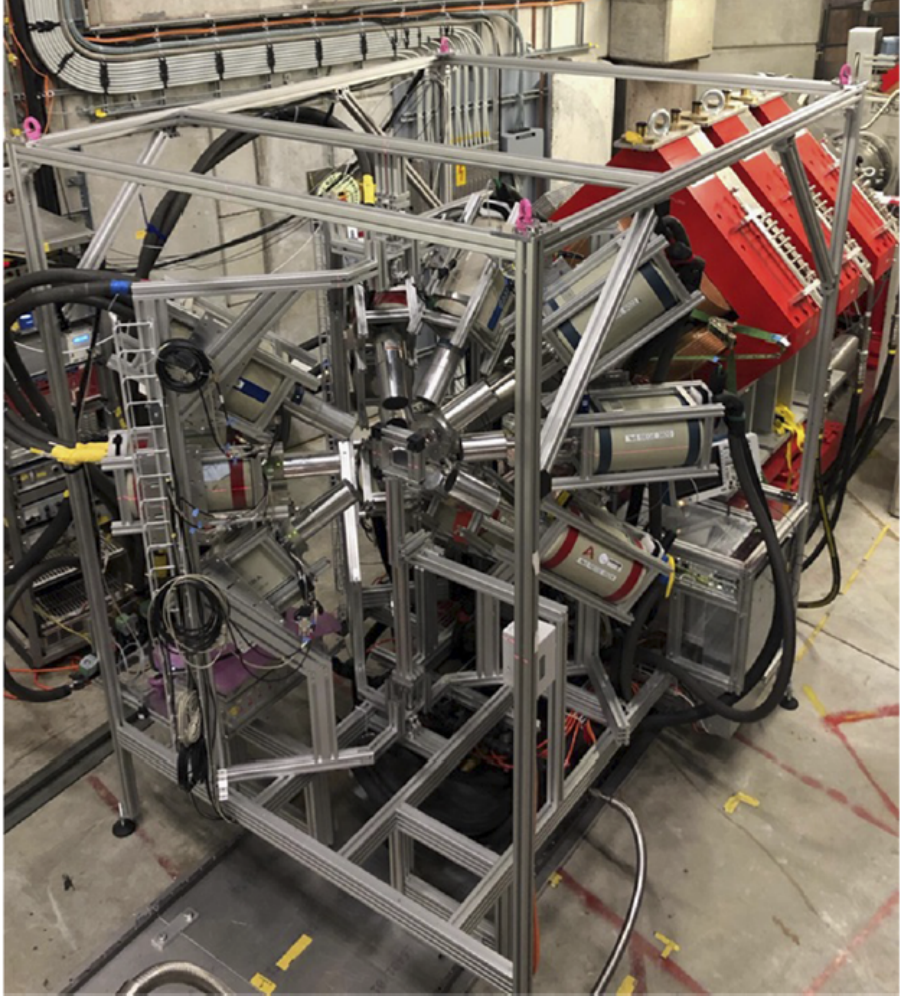


Figure 1: The GIANT setup for MIXE at the  $\pi$ E1 beamline at PSI. The muon beam is transported in the vacuum chamber on the top-right, and shaped by a triplet of quadrupole magnets (red) in order to focus the muons onto the sample, located in the center of the High-Purity-Germanium (HPGe) detector array.

At the end of the stopping process in the sample, negative muons are captured in the Coulomb field of the positive charge of the target nucleus, creating a so-called muonic atom [1, 3, 2]. This capture will leave the muon-atom system in an excited state with the principal quantum number  $n_\mu \approx 14$  [7], which subsequently decays to the ground state within a picosecond resulting in the emission of characteristic X-rays. This emission process can be compared to electron-induced X-ray fluorescence, but at 207 times higher energies due to the larger muon mass. Fig. 2 depicts the 3 main processes of MIXE: muon implantation, muon capture, and muonic cascade.

An approximation of the X-ray energies released in this process may be computed using the Dirac equation, like for electronic transitions, but with the mass of the muon, 207 times larger than the electron. The energy range of muon-induced X-ray fluorescence is therefore around two orders of magnitude larger than that of electron-induced fluorescence. Elements heavier than vanadium all display K1-L3 emission lines with energies greater than 1 MeV. Such energetic photons, unlike

soft X-rays induced by electronic cascade, can traverse long distances in dense material, such as a metallic battery pouch [8, 9]. Computer codes such as Akylas[10] or MUDIRAC[11] can produce an extended database of typical X-ray photons, taking into account both isotopic and orbital differences. PHITS [12, 13, 14] and GEANT4 [15, 16] can compute these typical transitions and output a tentative muonic X-ray photon spectrum.

Once the captured negative muons reach the ground state, they either decay or undergo nuclear capture, especially in high-Z elements. This capture may additionally lead to gamma and/or neutron emission, either promptly or when the transmuted isotopes decay. These decays can be recorded for subsequent analysis and cross-verification of the isotope identified by MIXE.

Heavy elements ( $Z > 25$ ) display line splittings due to an isotopic shift on the order of several keV, allowing for easy non-destructive identification of isotopes. Using the ratio of  $K_{\alpha}$  X-ray line emissions of materials bombarded by negative muons, it is possible to assess the isotopic composition of the sample. This technique was successfully employed for the non-destructive determination of the geographic origin of lead (Pb) artifacts, as its isotopic composition varies with mining locations[17]. In this case, the  $K_{\alpha}$  energy lines are found to be around 6 MeV, minimizing self-shielding, thereby facilitating accurate analysis at greater depths.

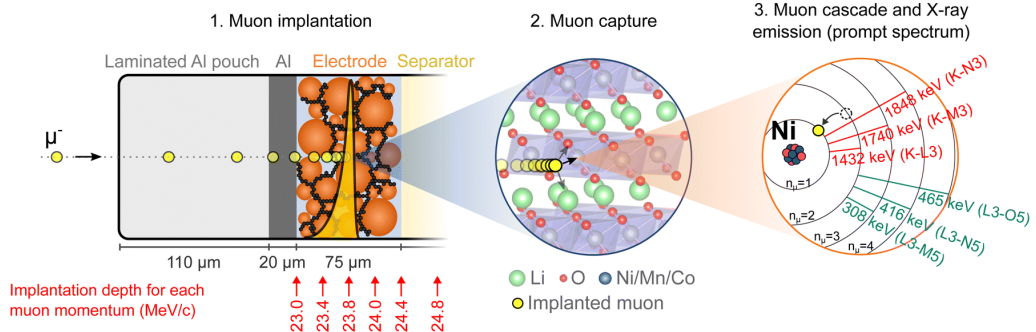


Figure 2: Steps to be modeled in PHITS: (1) negative muon transport from the beamline to the sample; (2) capture within the Coulomb field of a target atom; (3) muonic cascade with simultaneous emission of muonic X-rays. Image extracted from the work of Quérél et al. [18]

The sensitivity of MIXE to light isotopes (Na, Li) was first demonstrated in Japan [8, 9], and this result enabled a team from the Swiss Federal Laboratories for Material Sciences and Technology (Empa) to begin applying MIXE for in-situ, live, following of electrochemical processes inside battery packs [18]. These experimental setups and data will be implemented and compared to numerical models described below.

## 2. Materials and methods

### 2.1. Experimental geometry: the GIANT setup

The GIANT setup (Fig. 1) consists of an aluminium frame hosting up to 30 high-purity germanium (HPGe) detectors, continuously cooled by a liquid nitrogen circulation system. Samples are analyzed in air, positioned 10–20 cm from the beamport window depending on detector heads placements. Negative muons from the High-Intensity Proton Accelerator (HIPA) [5] are transported by the  $\pi$ E1 beamline and focused by a quadrupole triplet onto a plastic scintillator tagger (BC-400,  $21 \times 22 \text{ mm}^2$ ,  $200 \mu\text{m}$  thick). The light output is read by Advansid NUV-series SiPMs, providing  $\sim 0.4$  ns timing resolution. After tagging, muons cross a  $10 \mu\text{m}$  titanium window into air before reaching the sample. Multiple scattering in these entrance materials slightly broadens the beam and increases angular divergence at the target.

### 2.2. Simulation tools and configuration

Muon slowing-down and capture were modeled using SRIM [19], PHITS [12, 13, 14], and GEANT4 [15, 16]. All three codes simulate muon deceleration via electronic and nuclear scattering to estimate stopping profiles within the layered lithium-ion battery cell described in Ref. [18].

#### SRIM.

Since SRIM does not natively support muons, pseudo-muons were modeled as protons with rescaled mass  $m_\mu = 105.7/931.5 \simeq 0.113$  amu. Because SRIM’s stopping powers scale with  $Z^2$  and rely on Coulomb scattering, this approximation reproduces muon energy loss reasonably well while avoiding charge-exchange artifacts. Despite its limitations, SRIM (and TRIM.SP) has been successfully applied to positive-muon transport in thin films [20], and here serves as a lightweight benchmark for MIXE energies. Importantly, SRIM offers no possibility to simulate realistic beam optics: only monoenergetic, pencil-like beams incident on semi-infinite targets can be used.

#### PHITS and GEANT4.

Recent improvements in the PHITS muon-interaction module [21] motivated its benchmarking against GEANT4, the reference toolkit for particle transport. Muon capture cross sections were taken from Suzuki *et al.* [22], and the ensuing muonic X-ray cascade was simulated using the Akylas–Vogel routine [10]. Each code modeled the same simplified geometry (Fig. 3), including the tagger, vacuum window, 10 cm air gap, and eight battery layers with densities and thicknesses

listed in Table 1. Beam momentum spreads of  $\pm 0.5\%$  around nominal momenta were implemented to reflect the  $\pi$ E1 beam characteristics. A nominally pencil-like muon beam was generated in both codes; however, the multiple scattering induced by the muon tagger results in a significantly broadened beam spot after 10 cm of air gap, effectively defining the incident profile on the sample.

All simulations were conducted using SRIM-2008/TRIM 2013, GEANT4 v11.2.1, and PHITS v3.34.

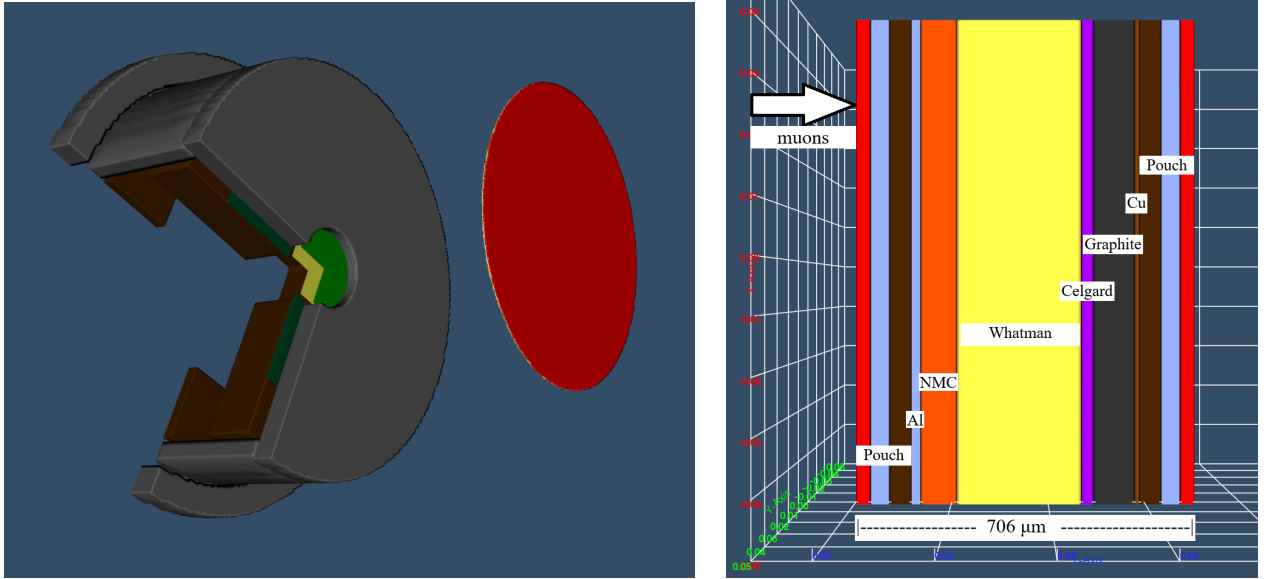


Figure 3: Left: PHITS geometry showing the muon beam (from left) through the tagger (yellow) and titanium window (green) before reaching the sample (red) 14 cm downstream. Right: Zoom on the multilayer battery stack. Material parameters are listed in Table 1.

Table 1: Thickness and density of the battery layers. The pouch is a polyamide–Al–polyethylene composite.

Layer	Pouch	Al	NMC	Whatman	Celgard	Graphite	Cu	Pouch
Density (g/cm <sup>3</sup> )	1.54	2.70	3.38	1.30	1.05	1.87	8.92	1.60
Thickness (μm)	115	20	75	260	25	86	10	115
Depth (μm)	115	135	210	470	495	581	591	706

### 2.3. Simulation scope and precision

PHITS offers multiple physics options for transport accuracy; the key cards used are listed in Appendix A. A sensitivity study showed that the `nspred` (Coulomb diffusion) flag alters implantation depth by less than 1%, indicating minimal angular-straggling influence under the present conditions. The GEANT4 application uses physics library `QGSP_BIC_HP_EMZ` and G4 material database.

Each run included  $2 \times 10^6$  primary muons for GEANT4 and PHITS. SRIM runs generated  $10^4$  pseudo-muons due to computational constraints. Output implantation profiles were averaged

over the final 5% of trajectories to derive the mean range and standard deviation. The results are compared quantitatively in the next section.

### 3. Results and discussion

#### 3.1. Negative muon implantation depths

A total of 56 muon energy groups were analyzed for their penetration and implantation depths within the modeled battery cell. The momentum limits were set by the lowest energy at which muons reach the target—many being stopped in the titanium window—and the highest energy where muons traverse the full stack without stopping. For GEANT4 and PHITS, momenta between 20 MeV/c and 30 MeV/c were simulated with up to  $2 \times 10^6$  primaries, after preliminary  $10^4$ -event runs to set boundaries of our energy scan range. SRIM results were obtained from  $10^4$  pseudo-muons. The mean implantation depths computed by each code are summarized in Tab. 2. While GEANT4 and PHITS results are nearly identical, SRIM exhibits significant

Table 2: Depths in  $\mu\text{m}$  of mean muon implantation in the battery, as computed by GEANT4 (reference), PHITS, and SRIM. Muons stopping in air before the battery are labeled "air".

P (MeV/c)	20	21	22	23	24	25	26	27	28	29	30
GEANT4	12.9	50.9	102.1	145.7	177.7	220.4	308.8	413.2	518.3	599.7	672.5
PHITS	13.0	49.0	96.8	146.0	176.5	216.9	309.5	405.9	510.4	595.7	675.1
SRIM	air	air	air	114	155	192	203	339	368	563	644

deviations, especially when large air volumes precede the thin-film stack. To isolate the origin of this discrepancy, the range of pseudo-muons in each battery layer was recalculated with SRIM and PHITS (Tab. 3). For isolated layers, SRIM and PHITS agree within 5%. Additional tests on upstream

Table 3: Ranges in  $\mu\text{m}$  of muons in individual battery layers at various momenta  $P$ , computed by PHITS (positive muons) and SRIM (pseudo-muons).

Layer P (MeV/c)	Pouch		Al		NMC		Whatman		Celgard		Graphite		Cu	
	20	30	20	30	20	30	20	30	20	30	20	30	20	30
PHITS	203	876	174	720	117	496	279	1193	331	1410	196	840	65	264
SRIM	205	873	169	700	115	485	274	1180	330	1410	196	831	63	252
Diff (%)	1.0	-0.3	-2.9	-2.8	-1.7	-2.2	-1.8	-1.1	-0.3	0.0	0.0	-1.1	-3.1	-4.5

materials (scintillator, titanium window, and various gases) confirmed this consistency (Tab. 4). The discrepancies in Tab. 2 stem from SRIM's averaging procedure. When a large low-density region precedes the target (e.g., air), the mean depth is dominated by those trajectories. Fitting

Table 4: Ranges in  $\mu\text{m}$  of muons in components along the beam path, computed by PHITS (positive muons) and SRIM (pseudo-muons).

Layer P (MeV/c)	He (m)		Air (m)		CO <sub>2</sub> (m)		BC400 (mm)		Ti ( $\mu\text{m}$ )	
	20	30	20	30	20	30	20	30	20	30
PHITS	1.87	8.23	0.32	1.37	0.21	0.88	0.33	1.40	117	478
SRIM	1.92	8.25	0.326	1.38	0.214	0.90	0.329	1.40	114	467
Diff (%)	2.67	0.24	1.88	0.73	1.90	2.27	0.30	0.00	2.56	2.30

the implantation tail with a Gaussian yields more realistic ranges consistent with PHITS, as shown in Fig. 4. The limited floating-point precision (5 digits, fixed  $\mu\text{m}$  unit) also restricts SRIM’s spatial resolution to  $\sim 10 \mu\text{m}$  over a 10 cm setup. Despite these limitations, SRIM remains useful for

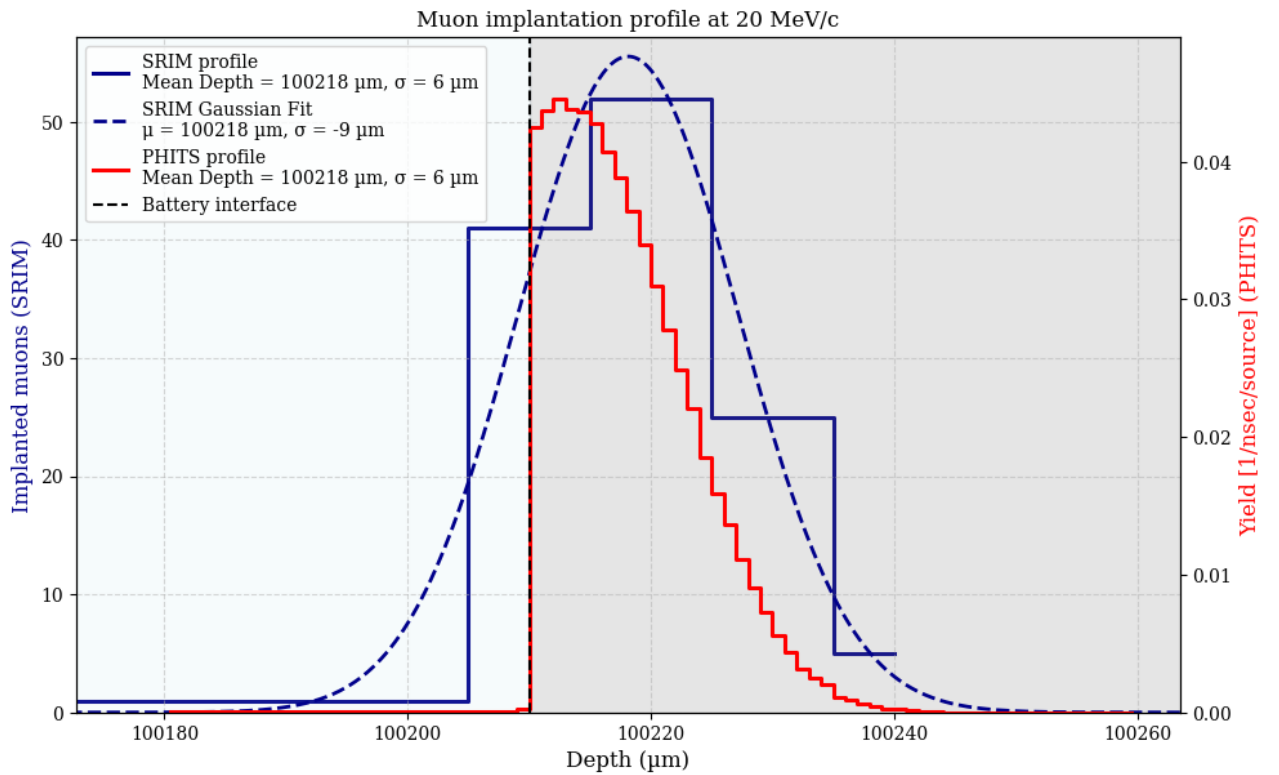


Figure 4: 20 MeV/c muon implantation profile as computed by SRIM (blue) for a 10 cm air cell (light blue) before the battery. The Gaussian fit (dashed line) yields  $100218 \mu\text{m}$  ( $R^2 = 0.97$ ), while SRIM’s internal mean is  $97570 \mu\text{m}$ . PHITS (red) highlights the density transition at the first PE layer (light grey).

preliminary range estimates. For subsequent analyses, only GEANT4 and PHITS were retained. The mean implantation depths from both codes are shown in Fig. 5. Excellent agreement ( $<1\%$ ) is achieved irrespective of PHITS’ *nspred* flag, indicating limited sensitivity to angular straggling. Momentum values between 23–28 MeV/c were thus selected for optimal probing between the Al and Cu electrodes. The residuals between codes (Fig. 6) show deviations only at low momentum, dominated by scattering in upstream layers.

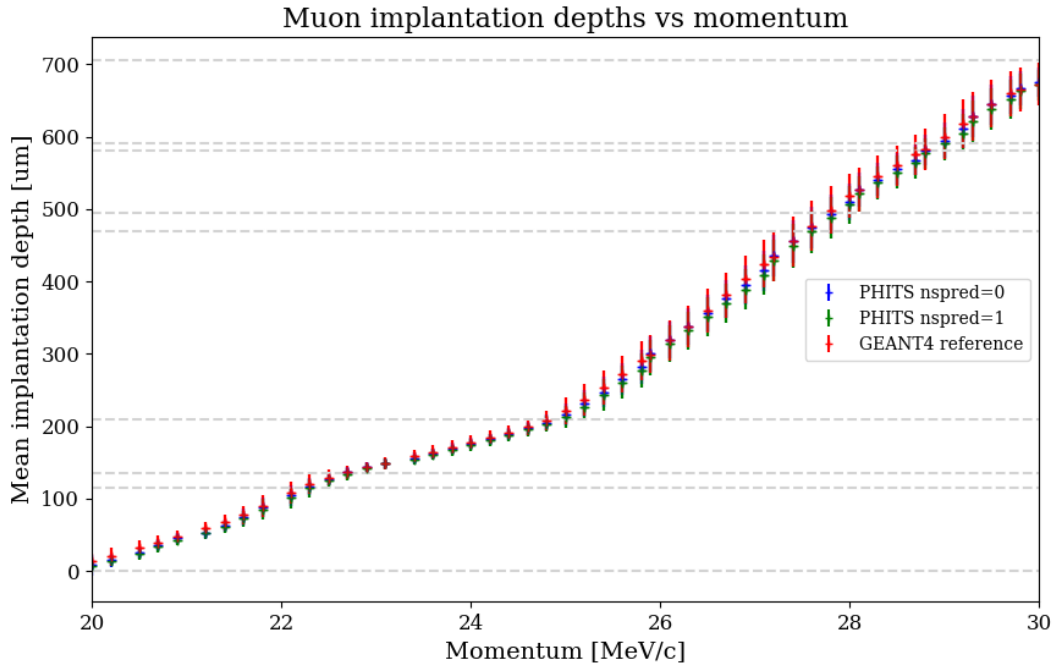


Figure 5: Simulated mean implantation depths of negative muons in the battery cell. Dashed lines indicate layer interfaces. Vertical markers translate the standard deviations of the mean implantation depth.

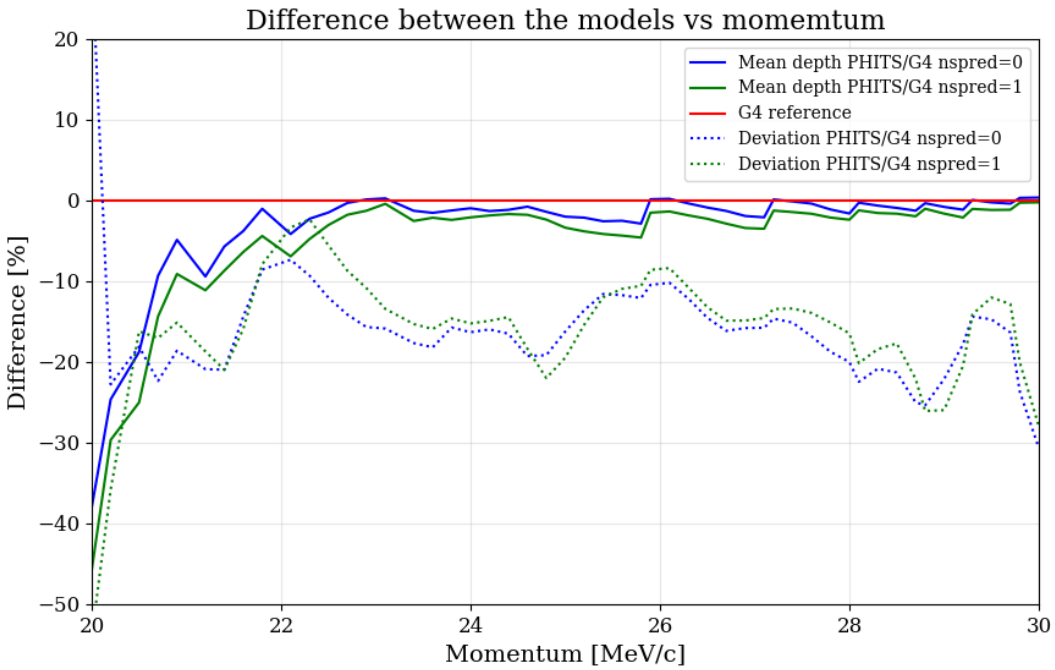


Figure 6: Solid lines: relative differences in mean muon implantation depth between PHITS and GEANT4 (reference). Larger deviations occur at low momentum due to scattering in air. Dashed lines: relative differences in standard deviation of the mean implantation depth as function of momentum, between PHITS and GEANT4 (reference).

The implantation profiles for several momenta (Fig. 7) illustrate these effects. Anomalous discontinuities—e.g., around 425  $\mu\text{m}$  in the Whatman layer at 27.4  $\text{MeV}/\text{c}$ —appear only with

*nspred*=1 and result from numerical inconsistencies in the slowing-down calculations of PHITS.

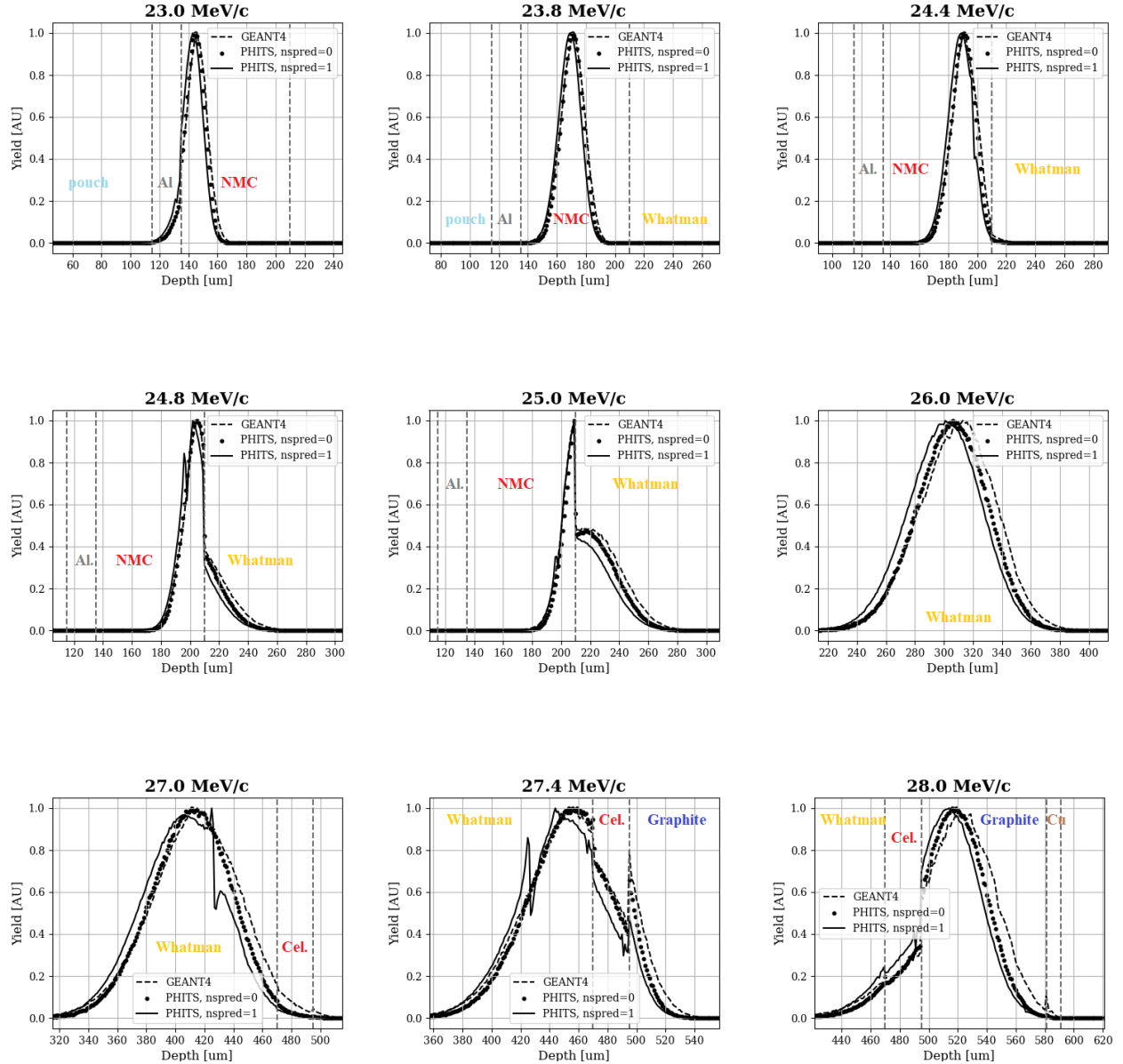


Figure 7: Implantation profiles of negative muon as a function of beam momentum. Results are presented with the GEANT4 results as a reference (dashed line) and for PHITS having the physics card *nspred* = 0 (dots) and *nspred* = 1 (solid line). Graphs are labeled with corresponding muon beam momenta.

### 3.2. X-ray emission from negative muon cascades

PHITS-computed photon spectra exhibit typical MIXE lines (Fig. 8), with low-energy  $K_{\alpha}$  transitions (C, Si, Al) well reproduced, while heavier elements (Ni, Mn, Co) show energy-shifted peaks. This issue is systematic across datasets. Comparison between PHITS (Akylas' code) and MUDIRAC reveals an increasing energy shift for high-Z elements (Fig. 9), reaching several hundred keV for Ni and Cu. The underlying cause was traced to an energy-scaling bug in *aama.f* routine

PHITS estimated MIXE spectrum at 23.8 MeV/c

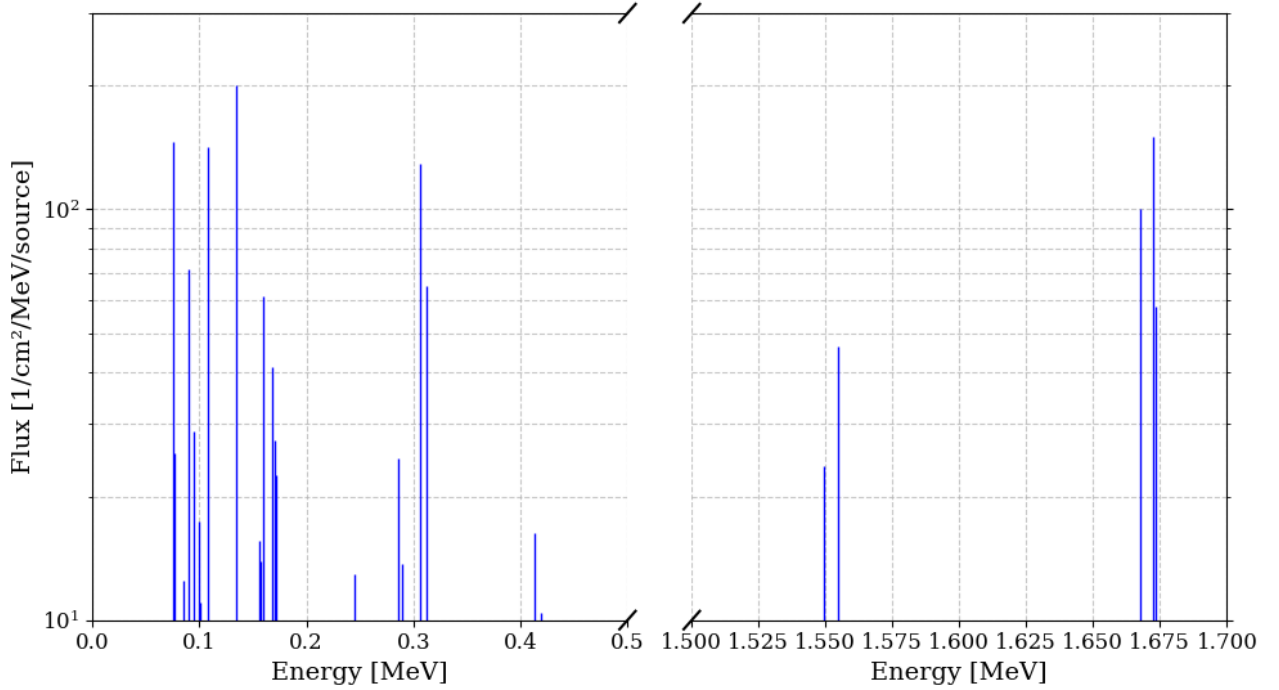


Figure 8: Raw MIXE emission spectrum from PHITS at 23.8 MeV/c. Low-energy peaks correspond to light elements K-lines MIXE signal and heavier elements (Mn, Ni, Co) L-lines. High-energy peaks corresponding to K-lines of the latter show shifted positions compared to reference data.

called by PHITS to compute the muonic X-ray cascade. The relative shift is shown in Fig. 9, with detailed values in Tab. A.2. To pinpoint which peak is associated to each isotope, we ran single element test run with 16 different targets. A dump file, called by modifying PHITS executable, would output the detailed cascade generated by *aamaa.f*, including transition levels, energies and intensities. It is noteworthy to mention that all hydrogen atoms had to be swapped for helium ones to avoid crashing of the *aama.f* routine, translating a pointer addressing issue in the atomic database. The slight modification of muon stopping power in virtual helium polymers has little impact on the scope of this assessment.

After identifying these systematic offsets, the relevant peaks were isolated in the composite spectrum (Fig. 10). The evolution of MIXE peaks with momentum reflects how the muons progressively penetrate deeper into the battery layers. At low momentum, only Al lines are visible, followed by Ni, Mn, Co, and Si as muons penetrate deeper. Cu K-lines emerge only at 28 MeV/c, in line with experimental findings. The evolution of K-line intensities with momentum is plotted in Fig. 11. While PHITS reproduces general spectral trends, absolute energies deviate from MUDIRAC, particularly for Ni and Cu isotopes (Tab. 5). MUDIRAC solves the Dirac equation for a bound muon in a finite-size nucleus using realistic nuclear charge distributions (typically

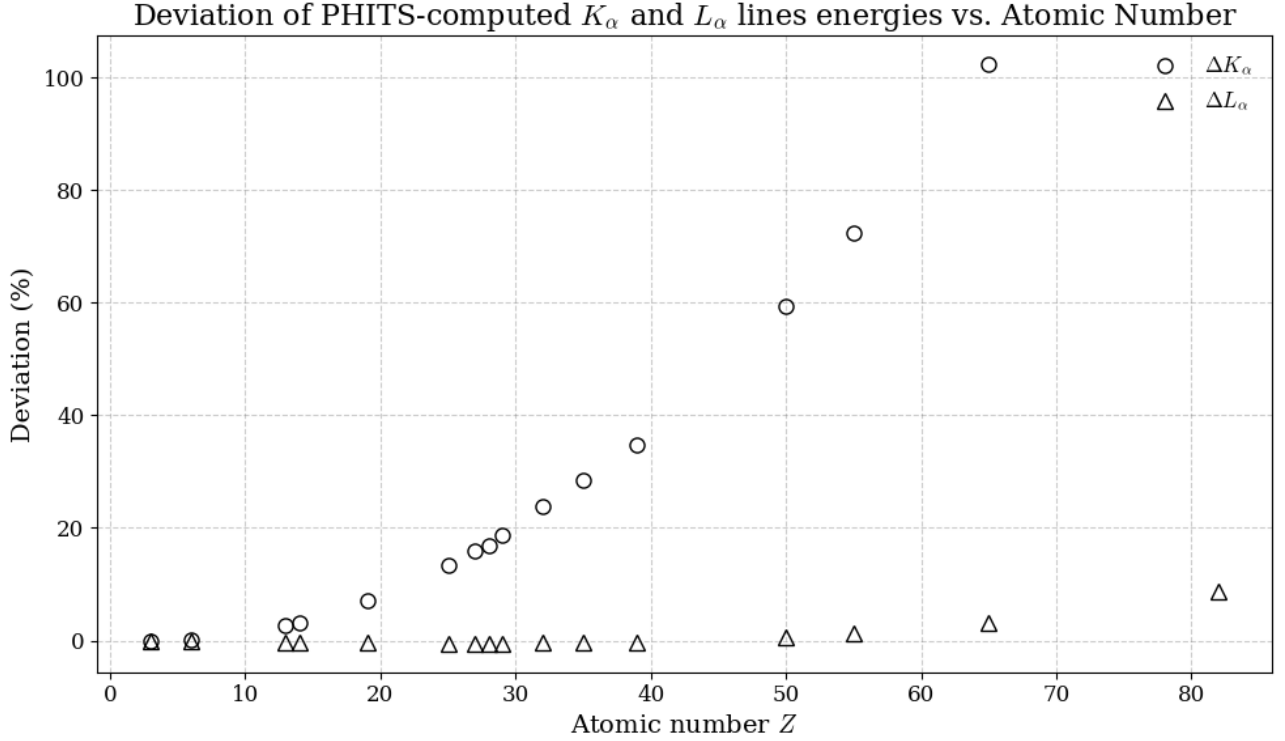


Figure 9: Relative energy shift between PHITS and MUDIRAC for K and L transitions. K-lines are more affected than L-lines, with the discrepancy increasing with  $Z$ .

Fermi or homogeneously charged spheres), and includes vacuum-polarization and relativistic recoil corrections at leading order. The code provides transition energies with sub-keV accuracy for medium- and high- $Z$  nuclei, and its predictions have been extensively benchmarked against precision muonic-atom X-ray measurements. PHITS underestimates isotopic energy shifts by nearly an order of magnitude compared to MUDIRAC and measurements.

Table 5: Energies in keV of some elements' muonic K-L transitions, as computed by MUDIRAC and PHITS.

Isotope	Line	Mudirac	PHITS
<sup>58</sup> Ni	K $\alpha_1$	1432.42	1672.99
<sup>58</sup> Ni	K $\alpha_2$	1426.90	1667.10
<sup>60</sup> Ni	K $\alpha_1$	1429.28	1673.10
<sup>60</sup> Ni	K $\alpha_2$	1423.75	1667.20
<sup>63</sup> Cu	K $\alpha_1$	1514.27	1796.66
<sup>63</sup> Cu	K $\alpha_2$	1507.95	1789.86
<sup>65</sup> Cu	K $\alpha_1$	1512.37	1796.76
<sup>65</sup> Cu	K $\alpha_2$	1506.05	1789.96

The transition energies of nickel K-lines measured experimentally (Fig. 12) agree closely with the predictions of MUDIRAC. A Gaussian decomposition performed on K and L lines groups (Tab. 6) shows consistent energy spacing and intensity ratios across isotopes. The areas of these

Gaussian curves will be used to estimate the ratio of intensities between K and L emission lines. The ratio  $R = K\alpha_2/K\alpha_1 = 0.5$  from PHITS was used to constrain Gaussian amplitudes, resulting in excellent fits to corrected K-line data. The L-lines around 308 and 313 keV exhibit similar proportionality. From the ensemble of Gaussian fits on the experimental data, the intensity ratio of nickel isotopes for  $K_\alpha/L$  was calculated. It yields 3.72, while PHITS returns 1.59. This simulated value is encouraging, as few models have demonstrated a relative intensity ratio of the same order of magnitude as the measurements.

Table 6: Parameters of Gaussian functions fitted to the Nickel spectra in Fig. 12. The instrument resolution  $\sigma$ , in keV, was set to 1.32 (K-lines) and 1.10 (L-lines).

Isotope	Line	Average (keV)	Area (AU)
<sup>58</sup> Ni	$K\alpha_1$	1432.42	8.13
<sup>58</sup> Ni	$K\alpha_2$	1426.90	4.06
<sup>60</sup> Ni	$K\alpha_1$	1429.28	3.13
<sup>60</sup> Ni	$K\alpha_2$	1423.75	1.56
<sup>62</sup> Ni	$K\alpha_1$	1426.84	0.43
<sup>62</sup> Ni	$K\alpha_2$	1421.32	0.22
<sup>61</sup> Ni	$K\alpha_1$	1428.36	0.14
<sup>61</sup> Ni	$K\alpha_2$	1422.84	0.07
Ni (all)	L3-M5	308.34	3.07
Ni (all)	L2-M4	313.30	1.69

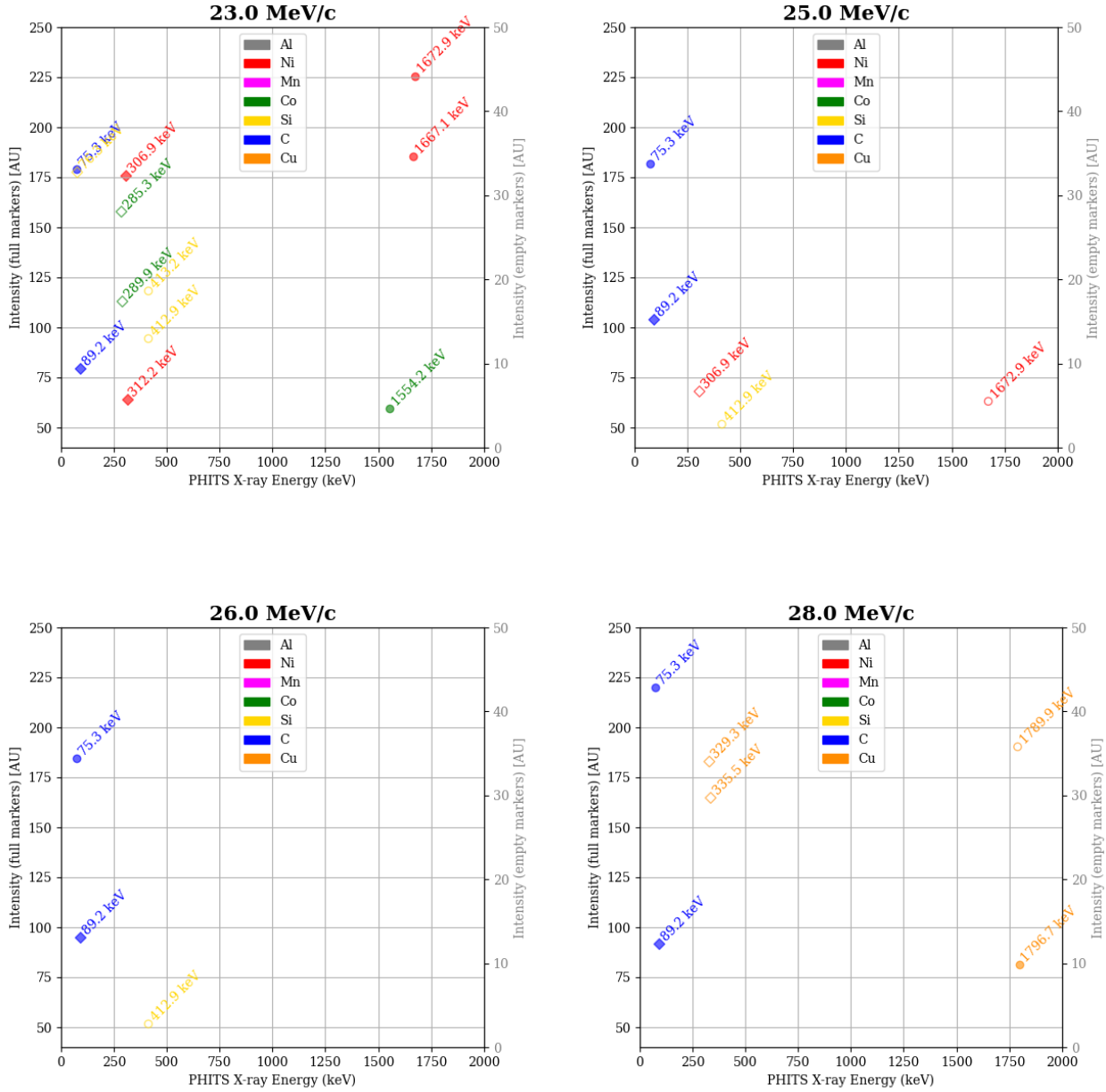


Figure 10: MIXE signal as estimated by PHITS for various momenta in the test battery. X-ray intensities are reported in Arbitrary Units, energies in keV. Each layer constitutive element should appear at a given momenta/implantation depth, such as estimated on Fig.7.

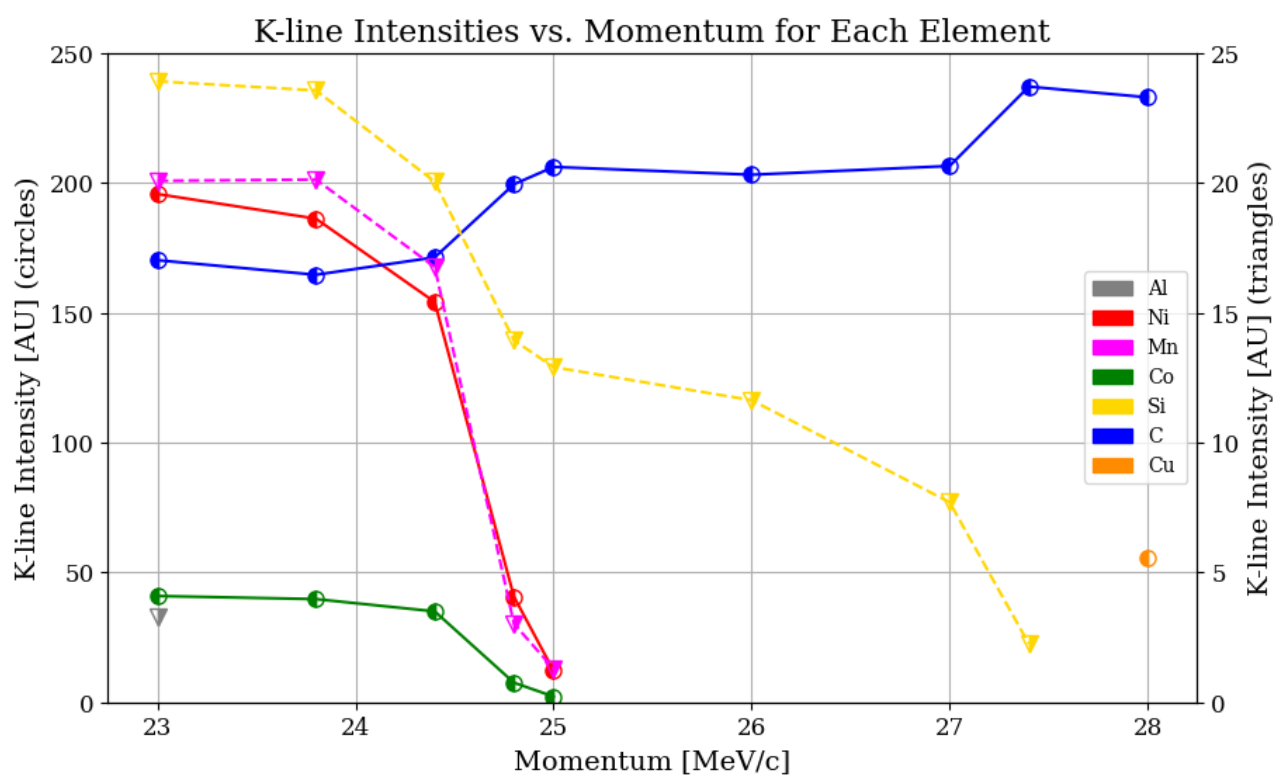


Figure 11: PHITS calculated K-line intensities (arbitrary units) versus beam momentum. Low-intensity lines are magnified by a factor of ten (dashed). Cu peaks appear only at the highest momenta.

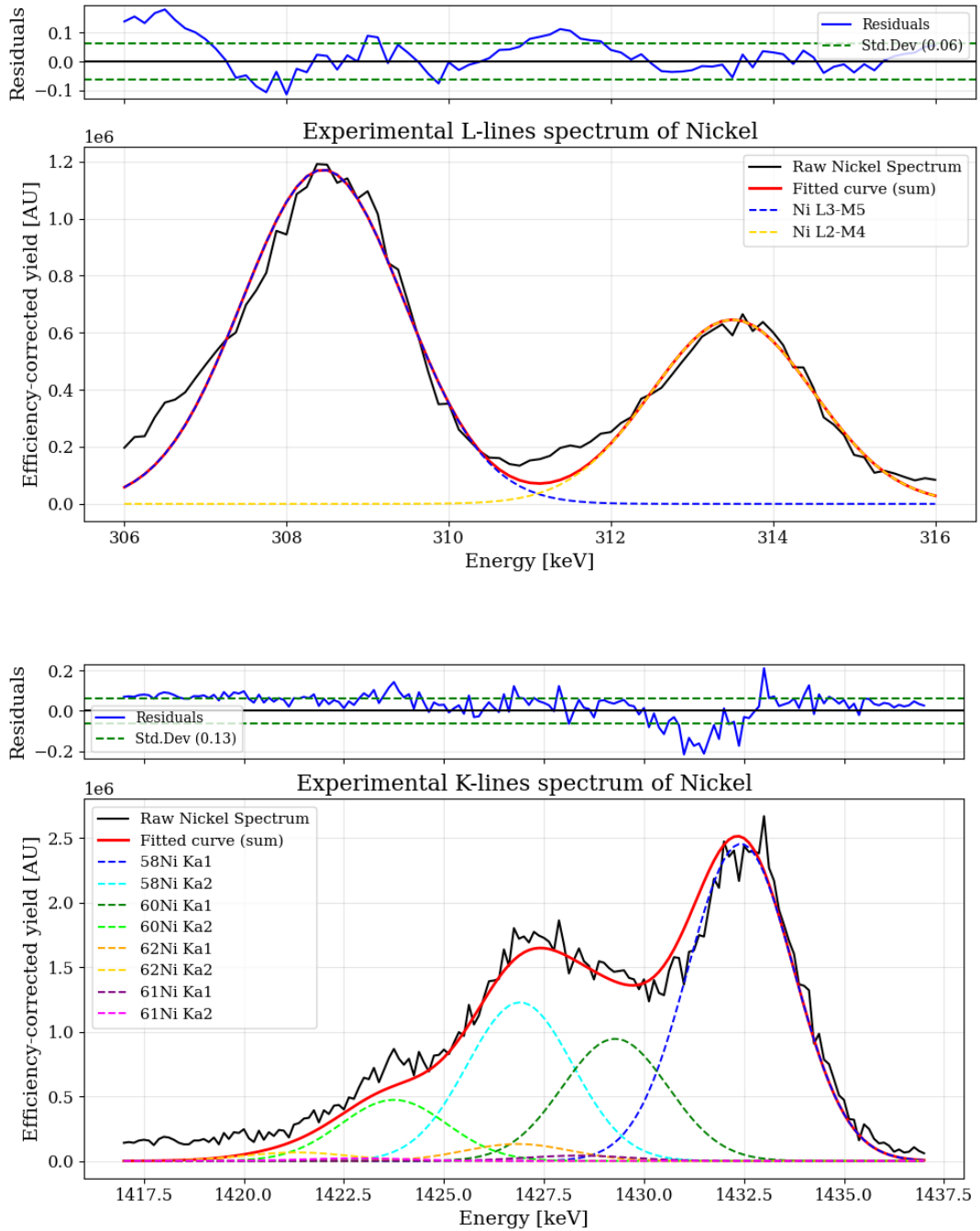


Figure 12: Measured nickel muonic x-ray emission spectrum as detected from the NMC layer of the battery at a momentum of 23.8 MeV/c. Isotopic shifts of  $^{58}\text{Ni}$  and  $^{60}\text{Ni}$  are clearly visible in the K-lines. Gaussian curves of each isotope K and L emission lines compose the function in red. Up: L lines. Down: K lines.

#### 4. Conclusion

A detailed benchmarking of GEANT4, PHITS, and SRIM has been conducted for the simulation of Muon-Induced X-ray Emission in a multilayer lithium-ion battery cell. GEANT4 and PHITS yield consistent predictions for implantation depths of negative muons, even in geometries with pronounced density contrasts, confirming their suitability for quantitative MIXE analysis. SRIM, while not originally intended for muon transport, remains a useful and rapid estimator of stopping ranges within individual layers, though its precision deteriorates when extended low-density materials such as air or other gases precede the target.

The modeling of muon capture and atomic cascades in PHITS reproduces relative line intensities with acceptable margins, but exhibits systematic energy shifts in K-line transitions of medium- to high-Z elements. This limitation currently prevents direct spectral comparison, yet the consistency of the predicted intensities underscores the reliability of the underlying cascade model. A practical remedy would be to couple PHITS to tabulated muonic-atom transition energies—either via lookup tables generated with MUDIRAC or by directly integrating the MUDIRAC routine into the PHITS atomic-cascade module—while retaining PHITS’ legacy cascade logic to compute relative intensities. Such a hybrid approach would substantially improve predictive accuracy.

Overall, SRIM and PHITS constitute efficient, user-friendly tools for predicting muon ranges and beam-momentum requirements in layered materials, while PHITS additionally enables preliminary spectral simulation. These results support the ongoing development of a web-based simulation platform for future MIXE users and provide a foundation for improving muonic-cascade modeling in next-generation versions of PHITS.

#### Appendix A: Supplementary Data

Table A.1: Key physics cards used in the set of PHITS simulations of the lithium-battery case.

Card	Parameter	Description
emumin	1.0e-3	minimum muon energy for nuclear reactions, in MeV
nspred	1	option for Coulomb diffusion (angle straggling)
nedisp	1	Energy straggling option for charges particles and nuclei
delt0	3e-4	max. step size if nspred =1
imubrm	0	muon-induced bremsstrahlung
imuppd	1	muon-induced pair-production
imuint	1	muon induced nuclear reaction with virtual photon theory
imucap	1	negative muon capture reaction and muonic X-ray emission
igamma	0	gamma photons generation and transport

Table A.2: Relative difference in energy between PHITS and MUDIRAC for various isotopes. Values are expressed as percentage deviations from MUDIRAC reference energies. PHITS values for heavy elements such as gold or lead could not be computed.

Isotope	$\Delta K_\alpha$ line (%)	$\Delta L_\alpha$ line (%)
<sup>7</sup> Li	-0.18	-0.16
<sup>12</sup> C	0.04	-0.16
<sup>27</sup> Al	2.64	-0.33
<sup>28</sup> Si	3.23	-0.35
<sup>39</sup> K	7.15	-0.43
<sup>55</sup> Mn	13.40	-0.47
<sup>58</sup> Ni	16.79	-0.47
<sup>59</sup> Co	15.90	-0.47
<sup>63</sup> Cu	18.65	-0.46
<sup>74</sup> Ge	23.72	-0.42
<sup>79</sup> Br	28.37	-0.36
<sup>89</sup> Y	34.85	-0.24
<sup>120</sup> Sn	59.45	0.55
<sup>133</sup> Cs	72.42	1.20
<sup>159</sup> Tb	102.24	3.05
<sup>208</sup> Pb	—	8.62

## References

[1] H. L. Anderson, C. Hargrove, E. Hincks, J. McAndrew, R. McKee, R. Barton, D. Kessler, Precise measurement of the muonic x rays in the lead isotopes, *Physical Review* 187 (4) (1969) 1565.

[2] F. Wauters, A. K. on behalf of the muX collaboration, The muX project, *SciPost Phys. Proc.* (2021) 022doi:10.21468/SciPostPhysProc.5.022.  
URL <https://scipost.org/10.21468/SciPostPhysProc.5.022>

[3] T. von Egidy, W. Denk, R. Bergmann, H. Daniel, F. J. Hartmann, J. J. Reidy, W. Wilhelm, Muonic coulomb capture ratios and x-ray cascades in oxides, *Phys. Rev. A* 23 (1981) 427–440. doi:10.1103/PhysRevA.23.427.  
URL <https://link.aps.org/doi/10.1103/PhysRevA.23.427>

[4] E. Köhler, R. Bergmann, H. Daniel, P. Ehrhart, F. Hartmann, Application of muonic x-ray techniques to the elemental analysis of archeological objects, *Nuclear Instruments and Methods in Physics Research* 187 (2) (1981) 563–568. doi:[https://doi.org/10.1016/0029-554X\(81\)90389-X](https://doi.org/10.1016/0029-554X(81)90389-X).  
URL <https://www.sciencedirect.com/science/article/pii/0029554X8190389X>

[5] J. Grillenberger, C. Baumgarten, M. Seidel, The High Intensity Proton Accelerator Facility, *SciPost Phys. Proc.* (2021) 002doi:10.21468/SciPostPhysProc.5.002.  
URL <https://scipost.org/10.21468/SciPostPhysProc.5.002>

[6] L. Gerchow, S. Biswas, G. Janka, C. Vigo, A. Knecht, S. M. Vogiatzi, N. Ritjoho, T. Prokscha, H. Luetkens, A. Amato, Germanium array for non-destructive testing (giant) setup for muon-induced x-ray emission (mixe) at the paul scherrer institute, *Review of Scientific Instruments* 94 (4) (2023).

[7] A. Knecht, A. Skawran, S. M. Vogiatzi, Study of nuclear properties with muonic atoms, *The European Physical Journal Plus* 135 (10) (2020) 777.

[8] I. Umegaki, Y. Higuchi, H. Nozaki, K. Ninomiya, M. K. Kubo, M. Tampo, K. Hamada, S. Doiuchi, P. Strasser, N. Kawamura, et al., Detection of li in li-ion battery electrode materials by muonic

x-ray, in: Proceedings of the 14th International Conference on Muon Spin Rotation, Relaxation and Resonance ( $\mu$ SR2017), 2018, p. 011041.

- [9] I. Umegaki, Y. Higuchi, Y. Kondo, K. Ninomiya, S. Takeshita, M. Tampo, H. Nakano, H. Oka, J. Sugiyama, M. K. Kubo, et al., Nondestructive high-sensitivity detections of metallic lithium deposited on a battery anode using muonic x-rays, *Analytical Chemistry* 92 (12) (2020) 8194–8200.
- [10] V. Akylas, P. Vogel, Muonic atom cascade program, *Comput. Phys. Commun.*;(Netherlands) 15 (3) (1978).
- [11] S. Sturniolo, A. Hillier, Mudirac: A dirac equation solver for elemental analysis with muonic x-rays, *X-Ray Spectrometry* 50 (3) (2021) 180–196.
- [12] K. Niita, T. Sato, H. Iwase, H. Nose, H. Nakashima, L. Sihver, Phits—a particle and heavy ion transport code system, *Radiation measurements* 41 (9-10) (2006) 1080–1090.
- [13] T. Sato, Y. Iwamoto, S. Hashimoto, T. Ogawa, T. Furuta, S.-I. Abe, T. Kai, Y. Matsuya, N. Matsuda, Y. Hirata, et al., Recent improvements of the particle and heavy ion transport code system—phits version 3.33, *Journal of Nuclear Science and Technology* 61 (1) (2024) 127–135.
- [14] Y. Iwamoto, S. Hashimoto, T. Sato, N. Matsuda, S. Kunieda, Y. Çelik, N. Furutachi, K. Niita, Benchmark study of particle and heavy-ion transport code system using shielding integral benchmark archive and database for accelerator-shielding experiments, *Journal of Nuclear Science and Technology* 59 (5) (2022) 665–675.
- [15] S. Agostinelli, J. Allison, K. a. Amako, J. Apostolakis, H. Araujo, P. Arce, M. Asai, D. Axen, S. Banerjee, G. Barrand, et al., Geant4—a simulation toolkit, *Nuclear instruments and methods in physics research section A: Accelerators, Spectrometers, Detectors and Associated Equipment* 506 (3) (2003) 250–303.
- [16] M. Cataldo, O. Cremonesi, S. Pozzi, E. Mocchiutti, R. Sarkar, A. D. Hillier, M. Clemenza, The implementation of mudirac in geant4: A preliminary approach to the improvement of the simulation of the muonic atom cascade process, *Condensed Matter* 8 (4) (2023) 101.

[17] K. Ninomiya, T. Kudo, P. Strasser, K. Terada, Y. Kawai, M. Tampo, Y. Miyake, A. Shinohara, K. M. Kubo, Development of non-destructive isotopic analysis methods using muon beams and their application to the analysis of lead, *Journal of Radioanalytical and Nuclear Chemistry* 320 (2019) 801–805.

[18] E. Quérel, S. Biswas, M. Heiss, L. Gerchow, Q. Wang, R. Asakura, G. Müller, D. Das, Z. Guguchia, F. Hotz, et al., Unlocking the probing-depth dilemma in spectroscopic analyses of batteries with muon-induced x-ray emission (mixe), *Journal of Materials Chemistry A* (2025).

[19] J. F. Ziegler, M. D. Ziegler, J. P. Biersack, Srim—the stopping and range of ions in matter (2010), *Nuclear Instruments and Methods in Physics Research Section B: Beam Interactions with Materials and Atoms* 268 (11-12) (2010) 1818–1823.

[20] E. Morenzoni, H. Glückler, T. Prokscha, R. Khasanov, H. Luetkens, M. Birke, E. Forgan, C. Niedermayer, M. Pleines, Implantation studies of kev positive muons in thin metallic layers, *Nuclear Instruments and Methods in Physics Research Section B: Beam Interactions with Materials and Atoms* 192 (3) (2002) 254–266.

[21] S.-i. Abe, T. Sato, Implementation of muon interaction models in phits, *Journal of Nuclear Science and Technology* 54 (1) (2017) 101–110.

[22] T. Suzuki, D. F. Measday, J. Roalsvig, Total nuclear capture rates for negative muons, *Physical review C* 35 (6) (1987) 2212.